Rapidity dependence of nuclear modification factors and identified particle ratios in Cu+Cu collisions at $\sqrt{s_{NN}} = 200$ GeV

(Dated: January 3, 2014)

The BRAHMS collaboration has measured transverse momentum spectra of charged pions, kaons, and protons and antiprotons at rapidity 0 and 3 for Cu+Cu collisions at $\sqrt{s_{NN}} = 200$ GeV. Kinetic freeze-out parameters of the Cu+Cu system are investigated as a function of centrality by a simultaneous blast-wave model fit to the six spectra at each centrality and rapidity. As the centrality of the system increases the collective flow of the system increases and the temperature decreases. At forward rapidities the matter in the system has both a lower temperature and a weaker radial expansion and hence a lower transverse momentum per particle. The temperature and average flow velocity do not scale with the local particle density. As the number of participant nucleons increases the yield of both pions and kaons per participant increases faster for Cu+Cu collisions compared to Au+Au collisions. Pions and kaon yields with transverse momenta between 1.5 and 2.5 GeV/c are suppressed relative to scaled pp collisions. This suppression increases with centrality and is independent of rapidity. The suppression of the kaons is somewhat less than that of the pions. Conversely the baryons in this momentum range are enhanced relative to pp collisions at the same energy. This enhancement depends strongly on momentum and rapidity but only weakly on centrality. The ratio of kaons to pions increases with transverse momentum up to 1.5 GeV/c and then levels off. This ratio depends strongly upon rapidity. The ratio of (anti)protons to kaons increases with transverse momentum up to 2.0 GeV/c before leveling off. The enhancement of baryons to mesons increases with the centrality of the collisions and is strongest for protons at forward rapidities.

PACS numbers: 25.75.Gz

I. INTRODUCTION

Experiments at the Relativistic Heavy Ion Collider (RHIC) have been studying the properties of a deconfined state of matter created in collisions of heavy nuclei at very high energies. Originally predicted to be a weakly interacting gas of quarks and gluons (Quark Gluon Plasma, QGP in short) which are collectively referred to as partons, the experimental evidence from RHIC compellingly pointed to the formation of a state of matter with properties characteristic of a nearly perfect liquid and which, accordingly, came to be known as strongly interacting Quark Gluon Plasma or sQGP in short [1–4]. As the QGP cools it undergoes a phase transition back to normal hadronic matter.

The matter created in heavy ion collisions exists for a very short period of time and its properties can be studied only indirectly through the measurement of hadrons, leptons and photons. Hadrons from hard scattered partons are believed to probe the late stages of the dense medium while soft hadronic observables deliver information on the final freeze-out stage of the collision. The early and dense stage of the collision can be directly studied through measurement of leptonic and electromagnetic observables. A major challenge in the field of relativisitic heavy ion collisions is then to find signatures that are unique to the QGP as opposed to properties of ordinary hadronic interactions.

It is expected that the signals from a deconfined phase should become stronger as the overlap region between the colliding nuclei increases. Investigating the difference between particle production in heavy ion collisions and elementary particle collisions is an important aspect of the research for the quest to understand the characteristics

of the matter created in heavy ion collisions. Thus, the system size dependences of spectral shapes, hadron yields and their suppression, and particle ratios are some of the many observables that need to be studied in order to gain insight into the effect of the system size and shape of the overlap zone on the evolution of the matter created in the collisions. The measurement of the observables mentioned above in Au+Au collisions at $\sqrt{s_{NN}}$ = 200 GeV has played a crucial role in characterizing the medium created in high-energy, nucleus-nucleus collisions. However, the study of the centrality dependence of these observables was limited to $N_{part} > 60$ leaving room for different scenarios of the N_{part} dependence of particle production in the large gap between the most peripheral Au+Au and p+p collisions. In order to extend the medium size dependence of physical observables down to small systems such as dAu and pp, the Cu+Cu system, with $A_{Cu} \sim 60$, was selected since it provides a good overlap with peripheral Au+Au in terms of the number of participants. Also, the relative uncertainty in the fractional cross-section of Cu+Cu collisions is smaller compared to that in Au+Au collisions for the same number of participants. The overlap region in central Cu+Cu is spherical while that in Au+Au for the same number of participants has an almond shape, making it possible to explore geometry effects on the experimental observables. The core/corona model of Beccatini and Manninen [5] provides a mechanism for testing these effects since the ratio of core to corona depends upon the shape of the overlap region.

In this paper, we present transverse-momentum spectra, yields, $\langle p_T \rangle$, nuclear modification factor (R_{AA}) and ratios for identified charged hadrons ($\pi^{\pm}, K^{\pm}, p, \bar{p}$) based on transverse momentum spectra obtained with the BRAHMS spectrometers in Cu+Cu collisions at $\sqrt{S_{NN}}$ = 200 GeV. The spectra are measured at two rapidities $y \sim 0$ and $y \sim 3$ as a function of collision centrality. The results will be compared to those obtained in pp and Au+Au collisions at the same energy, rapidity and centrality.

II. THE BRAHMS EXPERIMENT

The BRAHMS Experiment consists of two small acceptance magnetic spectrometers, the Mid-Rapidity Spectrometer (MRS) and the Forward Spectrometer (FS), for particle tracking and momentum determination and a system of global detectors made up of Beam-Beam Counters (BBC), Zero Degree Calorimeters (ZDCs) and a Multiplicity Array (MA) for event characterization [6, 7]. The MRS uses two time projection chambers (TPCs), TPM1 and TPM2, with a magnet between them and time of flight (TOF) walls for particle identification (PID). The Forward Spectrometer (FS) has two TPCs (T1 and T2) and three Drift Chambers (DCs) with magnets between consecutive detectors. In the FS, PID is achieved by using a TOF wall behind T2 and a second TOF wall and a Ring Imaging Cherenkov (RICH) detector both placed after the third DC. The TPCs and DCs provide three dimensional space points which together with the momentum information provided by the magnets allow for particle tracking. The MRS is capable of rotating between 90° and 30° with respect to the beam pipe covering the rapidity interval from $y \sim 0$ to $y \sim 1.6$. The FS rotates between 15° and 2° and covers the rapidity interval from $y \sim 2.2$ to $y \sim 4.0$. For the data presented in this paper, the MRS was set at 90° and the FS was set at 4°. The settings correspond to $y \sim 0$, $y \sim 3$ respectively.

A. Event Selection

The centrality of the collisions is characterized with a multiplicity array (MA) which consists of an inner array of Si strip detectors forming a hexagonal barrel surrounding the beam pipe where the interactions occur and an outer array of scintillator tile detectors also forming a hexagonal barrel coaxial with the inner strip detector system. By measuring the energy loss of charged

particles that traverse the two arrays, the strip detectors and the tiles provide two semi-independent measurements from which the pseudo-rapidity dependence of the charged particle density can be deduced. A realistic GEANT simulation of the detector response is used in this determination to map energy loss to the corresponding number of primary particles. Reaction centrality is based on the distribution of charged particle multiplicities within the pseudo-rapidity range covered by the MA, $|\eta| < 2.2$. For a a given event the centrality was taken to be as the fraction of observed events with a greater integral charged particle multiplicity than that event. The HIJING model was used to estimate the number of peripheral events missed because they do not leave sufficient energy in the MA for detection.

The primary collision vertex position is determined to an accuracy of ∼1 cm based on the relative time-of-flight of fast ($\beta \approx 1$) particles hitting beam-beam counter arrays. The BBCs consist of Cherenkov detectors mounted on photomultiplier tubes and are located 220 cm on either side of the interaction region. The BBCs also provide the start time for the time of flight (TOF) measurements.

For this analysis, the events have been divided into four centrality classes ($0-10\%, 10-30\%, 30-50\%$ and $50-70\%$). Events within ±25 cm of the nominal vertex were selected. Since the spectrometer acceptance varies from one event to another due to changing vertex location, spectral analysis is carried out in vertex bins of 5 cm and the results are statistically averaged to obtain a final spectra.

B. Track Selection

Straight line track segments are determined by tracking detectors which are outside the magnetic field regions. Matching track segments across the analyzing magnets allows for the determination of the track's momentum using the vertical magnetic field, the length traversed in the magnetic field region, the polar angle of the tracks with respect to the matching plane, and the average vertical slope of the tracks. The matching plane is defined as the vertical plane that contains the perpendicular bisector of the line joining the effective edge entry and exit points of the tracks in the magnet. Once the momentum is known, the reconstructed tracks are projected toward the beam axis and checked for consistency with the collision vertex determined by the BBCs. A 3σ cut is applied about the mean of the distribution of differences between the projected track vertex and the BBC vertex along the beam direction. An elliptical cut of 3σ is applied to the x, y distributions of track intersections with the primary vertex plane. This plane is defined as the plane normal to the beam axis that contains the collision vertex. The rapidity cuts were $|y| < 0.1$ at mid-rapidity and $2.95 < y < 3.15$ at forward rapidity.

C. Particle Identification

In this analysis, the MRS time of flight and the FS RICH detectors have been used for PID at y = 0 and y = 3 respectively. The time of flight measurement with TOFW and knowledge of the flight path length allows one to determine β, which together with the momentum of a detected particle provides for particle identification according to the relation given by

$$\frac{1}{\beta^2} = \frac{m^2}{p^2} + 1 \ . \tag{1}$$

Particles of different masses fall on separate curves if $\frac{1}{\beta}$ is plotted versus momentum. The TOFW provides π/K separation up to a momentum of 2 GeV/c and K/p separation up to 3 GeV/c.

For the FS, the emission angle θ_c of the light radiated in the RICH detector along the particle path is constant and is given by

$$\cos\theta_c = \frac{1}{n\beta}, \tag{2}$$

where n is the index of refraction of the gas inside the RICH volume. A spherical mirror of focal length L was used to focus the light cones onto rings of radii

$$r = L \cdot \tan\theta \tag{3}$$

Once the radii of the rings are measured, the masses of the particles are deduced from the formula

$$r = L \tan\ [\cos^{-1}(\ \frac{1}{n}\sqrt{1+\frac{m^2}{p^2}}\ )\ ]. \tag{4}$$

The RICH can identify pions starting at 2.5 GeV/c, kaons starting around 8 GeV/c and protons (anti-protons) from 15 GeV/c. π/K separation extends up to 20 GeV/c and protons (anti-protons) can be identified up to 35 GeV/c.

Figure 1 (top) shows the distribution of $\frac{1}{\beta}$ *vs.* p for the MRS where $q = 1$ for positive particles and $q = -1$ for negative particles. For this analysis, tracks were required to have measured $\frac{1}{\beta}$ values within 3σ of the nominal values given by Eq.(1) at y= 0 for each particle species. The curves show the 3σ cuts around the nominal trajectories for the different particle species. Figure 1 (bottom) shows the distribution of radius r *vs.* p for the RICH. At y = 3, the tracks were required to have a RICH radius within 3σ of the nominal radius for a given species determined from Eqn. (4).

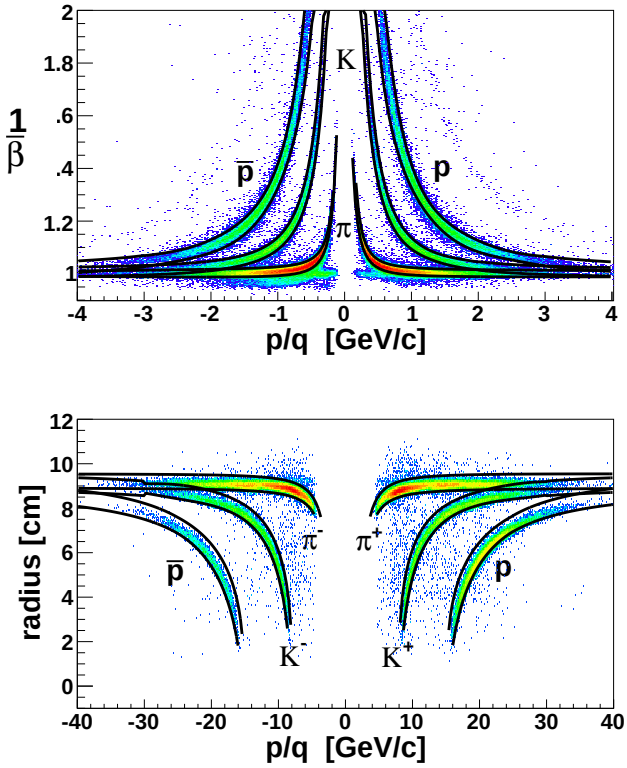

FIG. 1. Scatter plots of $\frac{1}{\beta}$ versus p/q (top) and RICH radius versus p/q (bottom) for Cu+Cu collisions at $\sqrt{s_{NN}} = 200$ GeV. The solid curves show the 3σ cuts around the nominal values given by Eqns. (1) and (4).

D. Corrections

The data presented here have been corrected for the geometrical acceptance of the spectrometers, tracking efficency, particle mis-identification and the effects of particle decays. The BRAHMS detector response is modeled using a realistic GEANT simulation of the experimental arrangement. This simulation is used to correct the experimental results for effects such as interactions with the beam pipe, absorption, and multiple scattering within the gas volumes of the tracking detectors.

The geometrical acceptance is accounted for using the GEANT Monte-Carlo simulations. Particles are "thrown" with a uniform momentum distribution over a range of angles $\Delta\phi$ and $\Delta\theta$ broad enough for the spectrometer aperture to lie within the range. The acceptance factor for a given pseudo-rapidity and p_T range is then the fraction of accepted particles to those thrown scaled by $\frac{\Delta\phi}{2\pi}$. This is done for each vertex bin and the different spectrometer angle and magnetic field settings. The acceptance correction is applied to the individual spectra from different spectrometer settings before they are averaged.

The tracking efficiency is calculated using the reference track method where good tracks from one detector are taken as input to a detector whose efficiency is sought. For the MRS, for example, tracks from the first time projection chamber (TPC) are used as input to determine the efficiency for the second TPC, and vice-versa.

The ratio of the number of tracks matching the reference tracks to the total number of input reference tracks is taken as the tracking efficiency. The product of the efficiencies calculated for the two MRS TPC's in this way is then taken to be the overall tracking efficiency for the MRS and is $\sim 92\%$. For the FS, the overall tracking efficiency is $\sim 80\%$. The systematic uncertainty on the final spectra associated with the determination of the tracking efficiency is $\sim 5-8\%$. The tracking efficiency is applied to the final MRS spectra. For the FS the efficiency correction was applied on a track by track basis.

To determine the GEANT based corrections, single particle events were processed through the standard BRAHMS analysis code. The simulations included multiple scattering and hadronic interaction processes. The GEANT corrections are applied on a track by track basis for both the MRS and FS.

To take into account particle mis-identification, a PID correction has been applied to the pion and kaon spectra. The systematic uncertainties on the PID corrections have been estimated by studying the distributions of m^2 *vs.* p (MRS and FS), $\frac{1}{\beta}$ *vs.* p (MRS), and r *vs.* p (FS). The PID corrections for the pions and kaons are shown in Tab. I, together with their uncertainties if they are significant. In the momentum range covered, the (anti)protons are well separated from the mesons and no PID correction is applied to their spectra.

	y=0		**y=3**	
	1.5 GeV	2.25 GeV	24 GeV	30 GeV
Pion	$< 1\%$	$15\% \pm 1\%$	$< 1\%$	$12\% \pm 5\%$
Kaon	$< 1\%$	$50\% \pm 5\%$	$< 1\%$	$25-30\% \pm 5\%$

TABLE I. PID correction factors and systematic uncertainties for pions and kaons at central and forward rapidity for various momenta.

III. RESULTS AND DISCUSSION

A. Identified particle spectra

Measurement of transverse momenta is the crucial first step in obtaining the various observables used to characterize the properties of the partonic medium created in heavy ion collisions. Figure 2 shows the invariant spectra for the charged hadrons $\pi^{\pm}, K^{\pm}, p$ and $\bar{p}$, versus transverse kinetic energy, for different collision centralities at $y \sim 0$ and $y \sim 3$. The spectra of particles and antiparticles have very similar shapes. Comparing pions, kaons and protons we see a steady hardening of the spectra with particle mass. Both of these effects are suggestive of hydrodynamics. The lines in Fig. 2 are fits of the hydrodynamically inspired Blast Wave model [8] to the six $\pi^{\pm}, K^{\pm}, p$ and $\bar{p}$ spectra at a given rapidity and centrality. These fits will be discussed in detail later. The magnitude of the spectra depend strongly on centrality for all particles and both rapidities. For kaons and protons the shape of the spectra harden as one moves from peripheral to central collisions. It is clear that the spectra of all particles are softer at forward rapidity but otherwise the trends observed with particle mass and centrality are similar at both rapidities.

We have done a systematic study of the spectra by fitting them to a variety of functions. The resulting fitting parameters, χ^2 per number of degrees of freedom, NDF, $\frac{dN}{dy}$, and $\langle p_T \rangle$ are listed in Tables V VI, and VII. For pions exponential functions in transverse momentum p_T ($Ae^{-\frac{p_T}{T}}$), transverse mass $m_T = \sqrt{m^2+p^2}$ ($Ae^{-\frac{m_T}{T}}$), and a power law function $A(1+\frac{p_T}{p_o})^{-n}$ where able to fit the data. The kaon spectra can be reasonably fit using exponentials in p_T, m_T or a Boltzmann function m_T ($Am_Te^{-\frac{m_T}{T}}$). For protons and antiprotons only exponentials in m_T and Boltzmann functions could describe the spectra.

For the pions, exponentials in p_T and m_T give similar results while the power law function results in larger

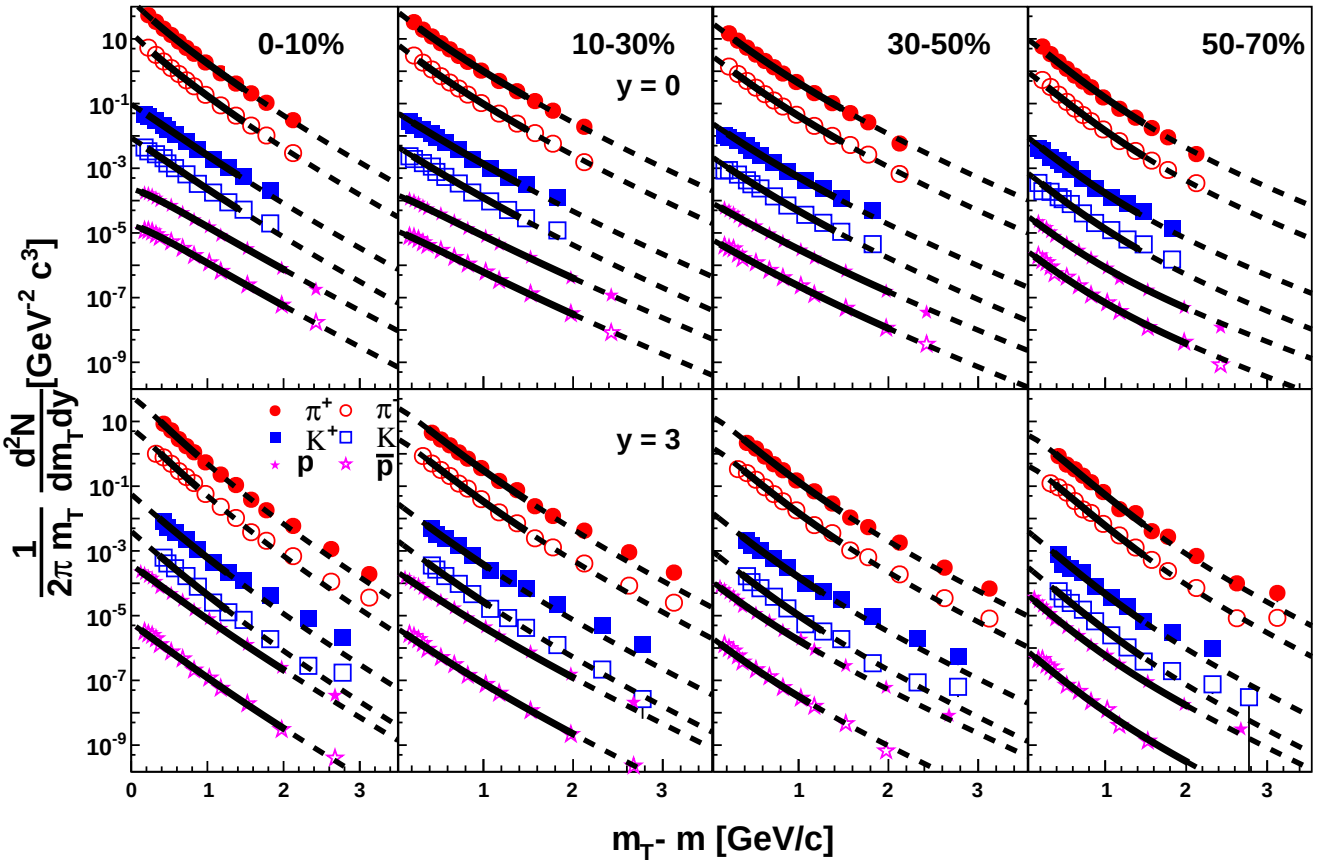

FIG. 2. Invariant spectra versus transverse kinetic energy at $y \sim 0$ (top panels) and $y \sim 3$ (bottom panels) as a function of centrality for $\pi^{\pm}, K^{\pm}, p$, and $\bar{p}$. The π^-, K^+, K^-, p and $\bar{p}$ spectra are scaled by factors of $10^{-1}, 10^{-2}, 10^{-3}, 10^{-4}$, and 10^{-5} respectively. The lines show the results of blast wave fits to each of the six spectra at a given rapidity and centrality. The solid lines indicate the fit range used while the dashed lines are extrapolations beyond the fit range. Only statistical errors are shown

values of $\frac{dN}{dy}$ and smaller values of $\langle p_T \rangle$. The power law function gives the best description of the pion data at central rapidity with χ^2/NDF much lower than for the exponential functions. At forward rapidity the χ^2/NDF values are similar for each of the three functional forms.

For the kaons, $(\frac{dN}{dy})_{p_T\ Exp.} > (\frac{dN}{dy})_{m_T\ Exp.} > (\frac{dN}{dy})_{m_T\ Boltz.}$ and $\langle p_T \rangle_{p_T\ Exp.} > \langle p_T \rangle_{m_T\ Exp.} > \langle p_T \rangle_{m_T Boltz.}$. The ranges of χ^2/NDF are similar for all three functions at both central and forward rapidity. For the protons and anti-protons, both the m_T exponential and the Boltzmann function give similar results for $\frac{dN}{dy}$ but $\langle p_T \rangle_{m_T\ Exp.} > \langle p_T \rangle_{m_T\ Boltz.}$. Both functional forms have similar χ^2/NDF values.

A model dependent analysis of the transverse momentum spectra as a function of rapidity and centrality allows the extraction of the thermodynamic and collective properties of the system at kinetic freeze-out. At mid-rapidity the hydro-inspired blast wave model [8] predicts a spectrum with

$$\frac{dN}{m_T dm_T} \sim \int_0^{R_{max}} dr\ \{r \times n(r) \times [m_T I_0(x) K_1(z)]\} \quad (5)$$

where $x = \frac{p_T}{T}\sinh(\rho)$, $z = \frac{m_T}{T}\cosh(\rho)$, $\rho = tan^{-1}(\beta_T)$, and $\beta_T(r) = \beta_s(\frac{r}{R})^{\alpha}$ is the velocity profile as a function of radial distance, r. For this study R was taken to be the nuclear radius. In Eqn. 6, $n(r)$ is the radial density profile. In this analysis $n(r)$ is assumed to have a Gaussian form $\sim e^{\frac{r^2}{2R^2}}$ for $r < R_{max}$ where $R_{max} = 3R$. For

$r > R_{max}, n(r) = 0$. The modified Bessel function $K_1(z)$ comes from integration from $-\infty$ to $+\infty$ over pseudo-rapidity η assuming boost invariance. At forward rapidity, the assumption of boost invariance is not valid and $K_1(z)$ should be replaced by integration over η over a finite range so that

$$\frac{dN}{dym_T dm_T} \sim \int_0^{R_{max}} dr\ \{r \times n(r) \times [m_T I_0(x) g(z)]\} \quad (6)$$

where

$$g(z) = \int_{\eta_{min}}^{\eta_{max}} \cosh(\eta - y)\ e^{-z\cosh(\eta - y)}\ d\eta \quad (7)$$

and y is the rapidity variable. The integration in Eqn. (7) was carried out, from $\eta_{min} = 2.4$ and $\eta_{max} = 4.4$.

For both the mid-rapidity and forward-rapidity data, we performed a simultaneous fit of the pion, kaon and (anti)proton spectra with 3 parameters: T, β_s, and α. The normalization parameters can be calculated from the data. Feed down from resonances was not considered as there are no data below 0.4 GeV/c. The fit range is restricted to $p_T < 1.8$ GeV/c for pions, $p_T < 2.0$ GeV/c for kaons since hard processes are expected to become significant above these momenta, and $p_T < 3.0$ GeV/c for (anti)protons. For the forward rapidity data, the forward spectrometer setting was at 4° , corresponding to $\eta = 3.4$. The fits are shown as lines in Fig. 2. The solid lines indicate the transverse mass (or momentum) range for the fits and the dotted lines are extrapolations using the extracted fit parameters.

Figure 3 shows the (anti-)correlation between the kinetic temperature and the average transverse velocity for several centralities at both rapidities. The numerical values from Fig. 3 are shown in Table II. As the centrality increases T_{kin} falls and β rises because the larger system stays together for a longer time. As the system cools random thermal motion of the partons is converted to bulk radial flow, lowering the temperature and increasing the average velocity. At y=3 the slope of the T_{kin} versus β curve is similar to that at y=0 but for a given β the temperatures are about 30 MeV lower.

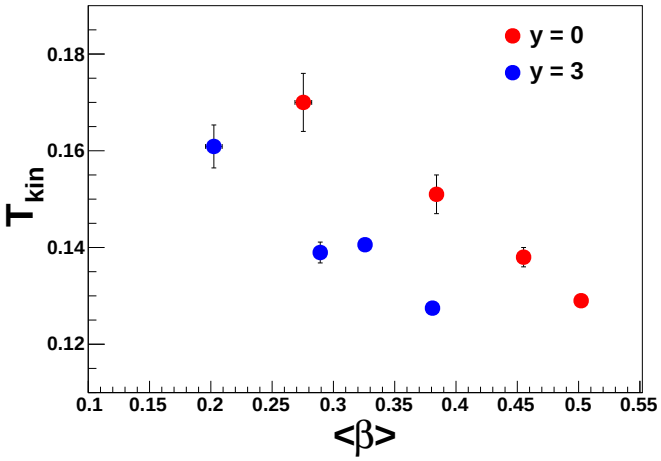

FIG. 3. Blast wave fit parameters T_{kin} vs. β_s for Cu+Cu collisions at $\sqrt{s_{NN}} = 200$ GeV. Centrality increases to the right.

This effect is not just due to the lower particle densities at y=3. Figure 4 shows the dependence of the effective temperature and the mean radial flow velocity for Cu+Cu and Au+Au collisions as a function of the total dN/dy ($\pi^{\pm}, K^{\pm}, p$ and $\bar{p}$) of each centrality class at a given rapidity. At a given dN/dy both T_{kin} and β are smaller at y = 3 reflecting the lower energy (and hence lower $\langle p_T \rangle$) that is available to the matter at forward rapidity

y = 0

Cent.	$\mathbf{T_{kin}}$**(MeV)**	$\langle$**b**$\rangle$	α	$\mathbf{x^2/dof}$
0 − 10%	129 ± 1	0.502 ± 0.002	0.494 ± 0.002	0.83
10 − 30%	138 ± 1	0.455 ± 0.002	0.599 ± 0.004	0.98
30 − 50%	151 ± 2	0.384 ± 0.004	0.786 ± 0.073	0.94
50 − 70%	170 ± 4	0.275 ± 0.007	1.28 ± 0.19	1.00

y = 3

Cent.	$\mathbf{T_{kin}}$**(MeV)**	$\langle$**b**$\rangle$	α	$\mathbf{x^2/dof}$
0 − 10%	128 ± 4	.378 ± 0.029	0.74 ± 0.19	0.99
10 − 30%	142 ± 5	.321 ± 0.030	0.91 ± 0.10	1.04
30 − 50%	141 ± 6	.289 ± 0.034	1.08 ± 0.11	1.00
50 − 70%	160 ± 8	.203 ± 0.060	1.534 ± 0.033	1.00

TABLE II. Blast wave fit parameters for Cu+Cu collisions at $\sqrt{s_{NN}} = 200$ GeV at various centralities at y = 0 (top) and y = 3 (bottom).

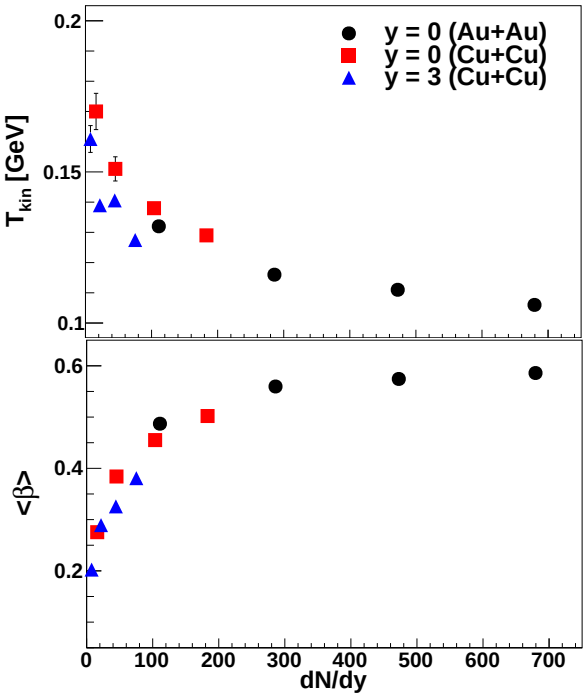

FIG. 4. T_{kin} (top) and $\langle\beta\rangle$ (bottom) for 200 GeV Au+Au collisions at y=0 and Cu+Cu collisions at y=0 and y=3 as a function of total $\frac{dN}{dy}$ ($\pi^{\pm}, K^{\pm}, p$ and $\bar{p}$) for various centralities.

The integrated yields are obtained by extrapolating outside the measurement region. The fraction of the particle yield within the BRAHMS acceptance varies from $30-75\%$ depending upon the spectrometer setting used. The $\frac{dN}{dy}$, $\langle p_T\rangle$, and fraction of particles in the BRAHMS acceptance are summarized in Tables III and IV. It should be noted that the results from the blast wave fit are in reasonable agreement with the results obtained by fitting the data to the simple functions discussed above.

In Fig. 5 dN/dy values scaled by N_{part} are shown for central (left panels) and forward (right panels) rapidity. Note, that the (anti)protons at $y = 0$ are corrected for contributions from Λ decays. The scaled dN/dy values from Cu+Cu join smoothly with those from Au+Au at $\sqrt{s_{NN}} = 200$ GeV, except for a slight excess of kaons and deficit of pions for Cu+Cu near $N_{part} \sim 50$. For comparison the STAR experiment finds that at $N_{part} =$ 99, Cu+Cu collisions produce $28\% \pm 12\%$ more K_0 than Au+Au collisions [9]. At both central and forward rapidity the kaon yields per participant pair are somewhat smaller for lower values of N_{part}. Beccatini and Manninen have proposed that such an effect could reflect the effect of two sources, a chemically equilibrated "core" and a "corona" of independent nucleon-nucleon collisions [5]. As the centrality of the system decreases the ratio of core to corona changes causing a change in the kaon yield per participant pair. A similar though less pronounced effect is seen in the proton and anti-proton yields.

Figure 6 shows the average transverse momenta $\langle p_T\rangle$ for pions, kaons and (anti)protons versus N_{part} for Cu+Cu collisions at y = 0 and y = 3 and for Au+Au collisions at y = 0. While the the pion $\langle p_T\rangle$ at y = 3 is similar to that at y = 0, the kaons and (anti)protons exhibit smaller values at forward rapidity. This drop in $\langle p_T\rangle$ for the heavier particles reflects the lower radial flow and freeze-out temperatures at forward rapidity shown in Figs. 3 and 4. The pion $\langle p_T\rangle$ appears to be independent of centrality, while the kaon and the (anti)proton $\langle p_T\rangle$ increases from peripheral to central Cu+Cu collisions at mid-rapidity. The pions and kaons show no dependence on centrality at forward rapidity while the (anti)proton $\langle p_T\rangle$ appears to increase with centrality. One can see that $\langle p_T\rangle$ increases with the particle mass indicating the heavier particles are more affected by radial flow than the lighter particles. The Cu+Cu data points join smoothly with those from Au+Au collisions (A similar result was observed by STAR for the K^{0*} [10].) This suggests that the transverse momenta are insensitive to the difference in shape of the Cu+Cu and Au+Au overlap regions for the same number of participants.

B. Nuclear Modification Factors

The discovery of hadron suppression at central rapidity in $\sqrt{s_{NN}} = 130$ GeV Au+Au collisions at RHIC has been one of the most exciting results in heavy ion physics [11–14]. These first measurements have since been extended to higher energies and lighter systems and also refined

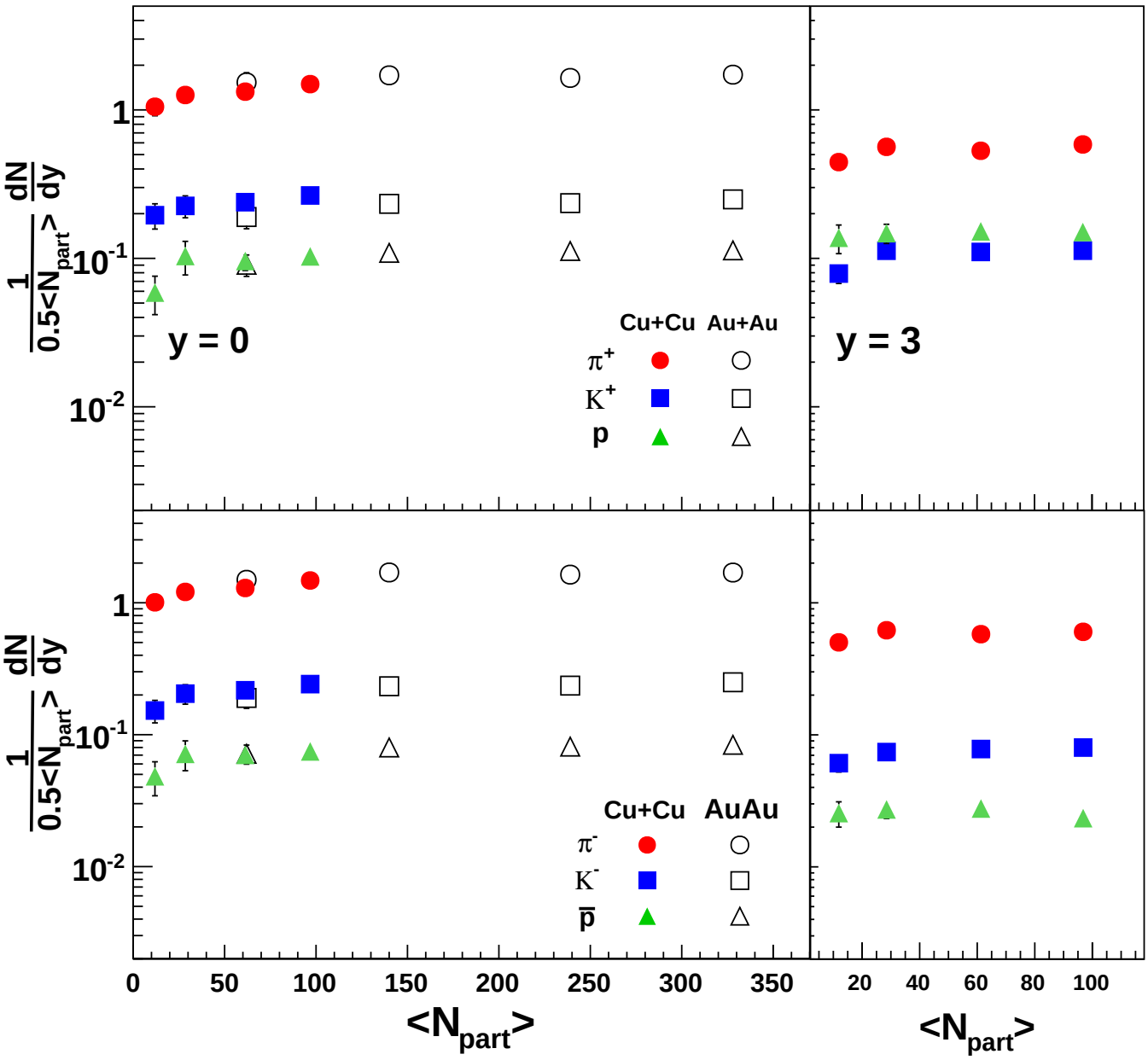

FIG. 5. N_{part} scaled $\frac{dN}{dy}$ for Cu+Cu and Au+Au collisions at $\sqrt{s_{NN}} = 200$ GeV as a function of N_{part} for at y = 0 (left) and y = 3 (right). Positive pions, kaons and protons are shown in the top panels while the antiparticles are shown in the bottom panels.

to include identified hadrons, heavy quarks and fully reconstructed jets [15–21]. Such effects have not be seen in d-Au collisions at RHIC [13, 14, 22, 23].

In central heavy ion collisions, suppression of hadrons at mid-rapidity is believed to be a consequence of the energy loss of partons in the dense medium formed in the collisions. The origin of the suppression at forward rapidity observed in 200 GeV d+Au and Au+Au collisions is not yet fully understood [13, 24].

The nuclear effects on particle production are studied in terms of the nuclear modification factor R_{AA} defined

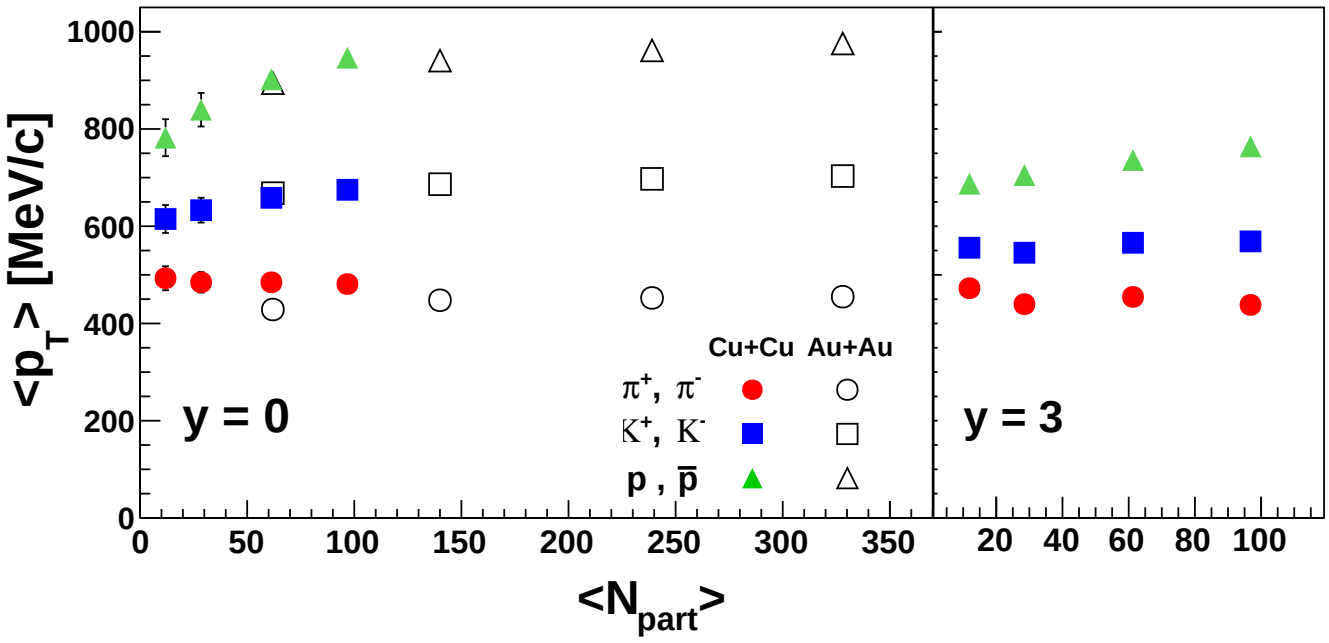

FIG. 6. Mean transverse momentum $\langle p_T \rangle$ for $\pi^{\pm}, K^{\pm}$, p and $\bar{p}$ as a function of N_{part} for Cu+Cu and Au+Au collisions at $\sqrt{s_{NN}} = 200$ GeV for y = 0 (left) and y = 3 (right)

as

$$R_{AA} = \frac{d^2N_{AA}/dp_T dy}{\langle N_{bin} \rangle d^2N_{pp}/dp_T dy} \quad (8)$$

which is the ratio of the particle yield in heavy ion collisions to the yield in pp collisions scaled by the average number of binary nucleon-nucleon collisions N_{bin} for a given centrality class. If AA collisions were just a superposition of elementary collisions between nucleons, then $R_{AA} = 1$.

Figure 7 shows the nuclear modification factor R_{AA} for pions, kaons and (anti)protons respectively in Cu+Cu collisions. The pion and kaon R_{AA} values are averages of the positive and negative particles. At low p_T, R_{AA} approaches the value of $\frac{N_{part}/2}{N_{bin}}$, suggesting that the bulk particle production is dominated by the number of participants in the collision.

The pion and kaon R_{AA} ratios above $p_T > 1$ GeV/c are suppressed with the effect being strongest for the pions. The level of suppression is strongest for more central collisions which achieve the highest densities. This is consistent with the fact that the multiplicity density decreases as one goes to more peripheral collisions; there is less matter to interact with and more partons make it out of the collision region before losing much of their energy. The kaon R_{AA} values show slightly less suppression than the pions but have a similar dependence on centrality. A similar effect is seen in preliminary data from the ALICE collaboration for Pb+Pb collisions at $\sqrt{s_{NN}} = 2.76$ TeV/c [25]. The difference in the pion and kaon suppression patterns may reveal information about the fragmentation functions [26]. At mid-rapidity, the R_{AA} values for pions and kaons vary little with p_T over the range $p_T = 1.5 - 2.5$ GeV/c. At forward rapidity there is an increase of the kaon and pion R_{AA} values. This p_T dependence is similar for all centralities. The significant suppression of pions and kaons in the p_T range covered by the BRAHMS results suggests that the effect of energy loss may extend to as low as 1.5 GeV/c in p_T which is quite removed from the hard processes regime

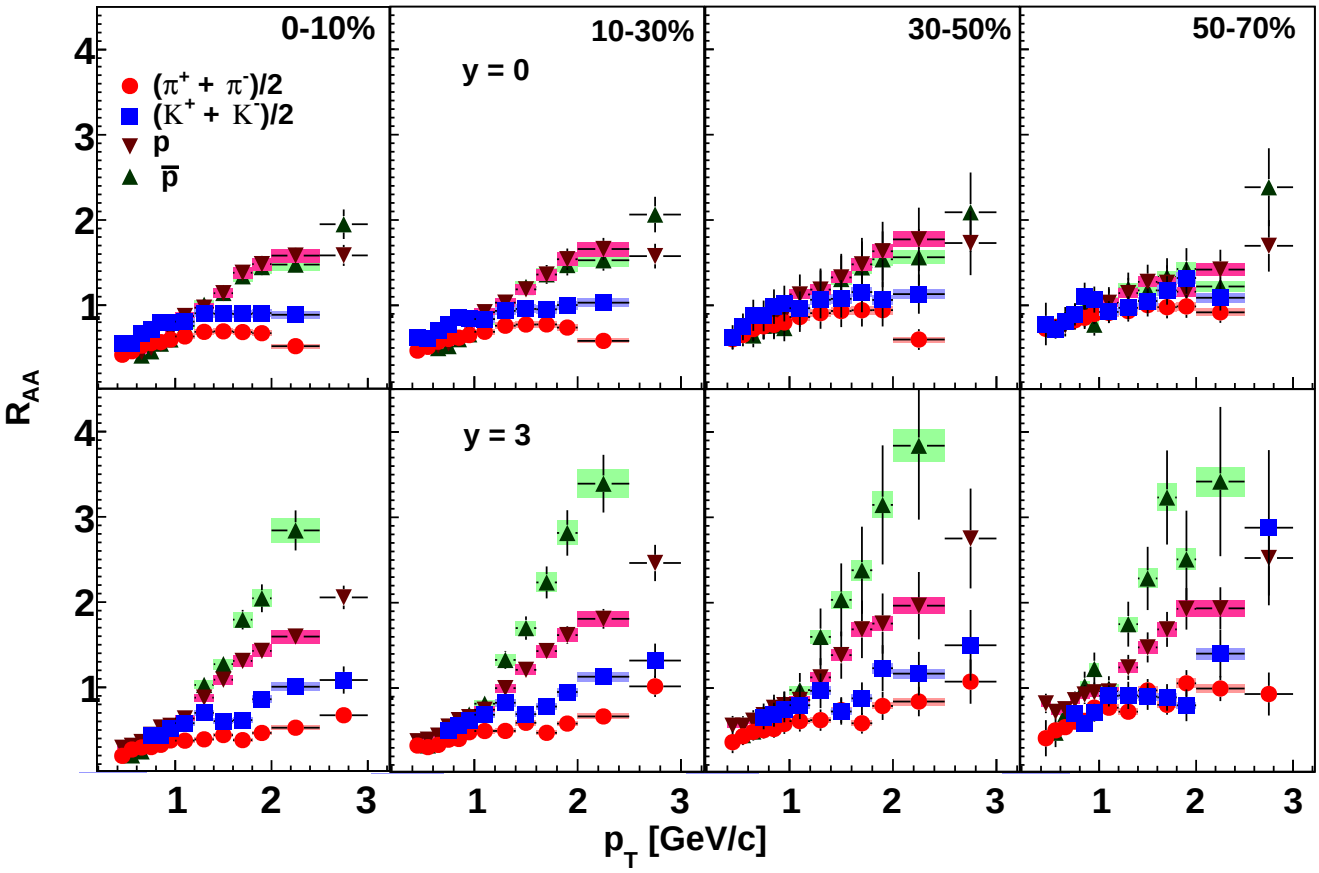

FIG. 7. Nuclear modification factor of $\sqrt{s_{NN}} = 200$ GeV Cu+Cu collisions for pions, kaons and (anti)protons as a function of p_T and centrality for rapidity = 0 (top) and forward rapidity (bottom). The centrality decreases from left to right.

($p_T > 6$ GeV/c).

For both protons and antiprotons R_{AA} rises steadily with p_T crossing 1.0 at $p_T \approx 1.3$ GeV/c for all centralities and both rapidities. The enhancement for $p_T > 1.3$ GeV/c is strongest in peripheral collisions and at forward rapidity. At central rapidity the enhancement is similar for protons and antiprotons but at y=3 the antiprotons show a greater enhancement than the protons. Note the STAR collaboration has measured R_{AA} for pions and $p+\bar{p}$ for Cu+Cu collisions at $\sqrt{s_{NN}} = 200$ GeV/c for $p_T \geq 3$ GeV/c R_{AA} [27]. These results are consistent with our highest p_T data points but fall steadily before leveling off at $p_T \approx 6$ GeV/c.

C. Particle Ratios

Figure 8 shows antiparticle to particle $\frac{dN}{dy}$ ratios of integrated yields measured in Cu+Cu and Au+Au collisions at $\sqrt{s_{NN}} = 200$ GeV/c as a function of the number of participants, N_{part}. The left panel is for $y \sim 0$ and the right panel for $y \sim 3$. As is seen, these ratios of integrated yields do not exhibit a centrality dependence at mid-rapidity. There is very little difference between the Cu+Cu and Au+Au results. At $y \sim 3$ there is a slight drop of the $\frac{\pi^-}{\pi^+}$ ratio with N_{part}.

Figure 9 shows the kaon to pion ratios (upper two panels) and baryon to meson ratios (lower two panels) as functions of p_T, centrality and rapidity. At mid-rapidity, the data show a linear increase at low p_T but seem to saturate for $p_T > 1.5$ GeV/c, with the $\frac{K^+}{\pi^+}$ ratio showing

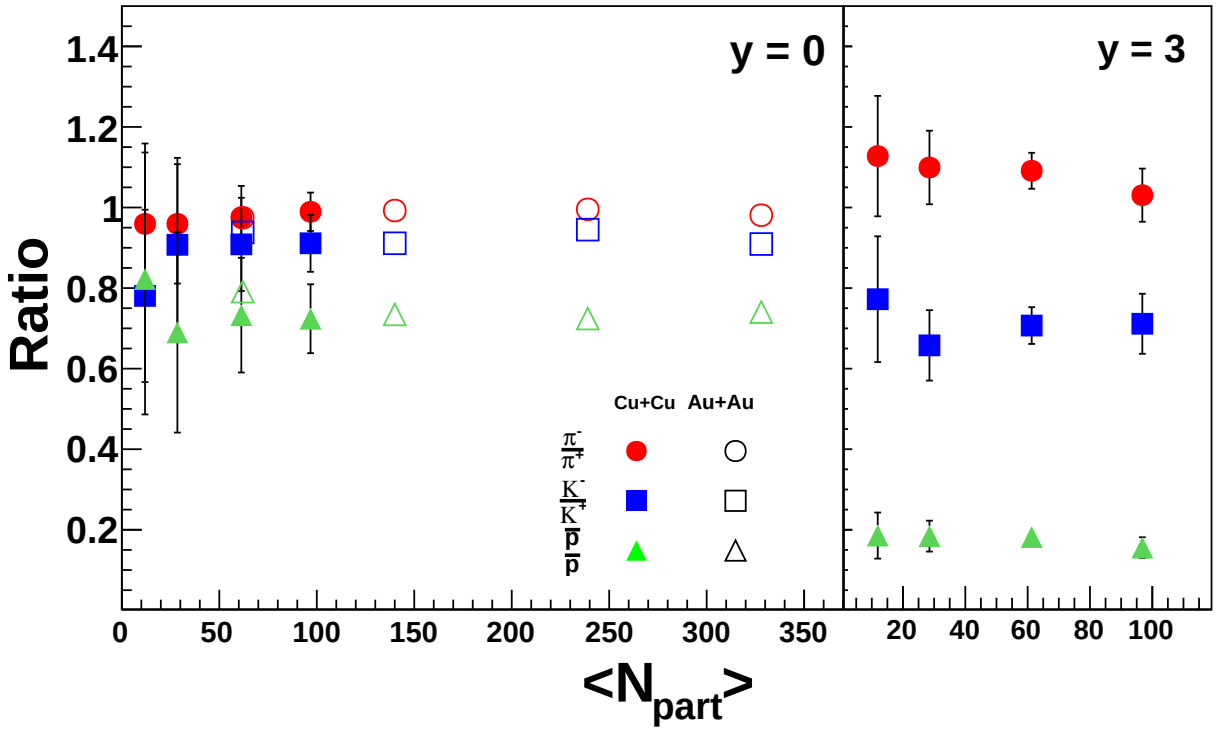

FIG. 8. Ratios of antiparticle/particle yields versus N_{part} for pions, kaons and protons at y = 0 (left) and y = 3 (right) for Cu+Cu and Au+Au collisions at $\sqrt{s_{NN}} = 200$ GeV.

only a slight excess over the corresponding $\frac{K^-}{\pi^-}$ values. At $y \sim 3$ the $\frac{K^+}{\pi^+}$ shows some centrality dependence and is significantly enhanced over the corresponding $\frac{K^-}{\pi^-}$ results.

An enhancement of baryons over mesons is observed at both rapidities. It has been shown before that the $\frac{p}{\pi}$ ratio at mid-rapidity approaches unity, contrary to what is observed in elementary particle collisions where the ratio does not exceed 0.2 in the corresponding momentum range for both quark and gluon jets. The fact that the $\frac{p}{\pi^+}$ and $\frac{\bar{p}}{\pi^-}$ ratios are close to unity in the intermediate p_T region for central collisions may be attributed to either quark coalescence [28–30] or baryon transport dynamics based on topological gluon field configurations [31–33].

The N_{part} dependence of the $\frac{K}{\pi}$ and $\frac{p}{\pi}$ ratios are displayed in Fig. 10 where the data have been integrated over $1.3 < p_T < 2.0$ GeV/c for y = 0 and over $1.5 < p_T < 3.0$ GeV/c for y = 3. The $\frac{K}{\pi}$ ratios show a dependence on centrality at mid rapidity, but this ratio seems to saturate at forward rapidity for mid-central to central events. The greater $\frac{K^+}{\pi^+}$ values as compared to the $\frac{K^-}{\pi^-}$ results may be attributed to the larger baryon density which increases the probability of associated production for K^+. At $N_{part} \sim 50$ the integrated $\frac{K^\pm}{\pi^\pm}$ ratios in Cu+Cu collisions are higher than those observed in Au+Au collisions for similar values of N_{part}, see Fig. 5. This is consistent with the observation by the STAR collaboration that the yield of strange mesons and baryons rises more quickly with N_{part} in Cu+Cu collisions compared to Au+Au [9] and is consistent with the core/corona model of [5].

The right hand side of Fig. 10 shows the $\frac{p}{\pi^+}$ and $\frac{\bar{p}}{\pi^-}$ ratios versus N_{part}. The ratios seem to exhibit a monotonic increase with N_{part}. At mid-rapidity the ratios are smaller than unity with $\frac{p}{\pi^+}$ values larger than the corresponding $\frac{\bar{p}}{\pi^-}$ values. At forward rapidity, the $\frac{p}{\pi^+}$ ratio is generally greater than unity and is larger than the corre-

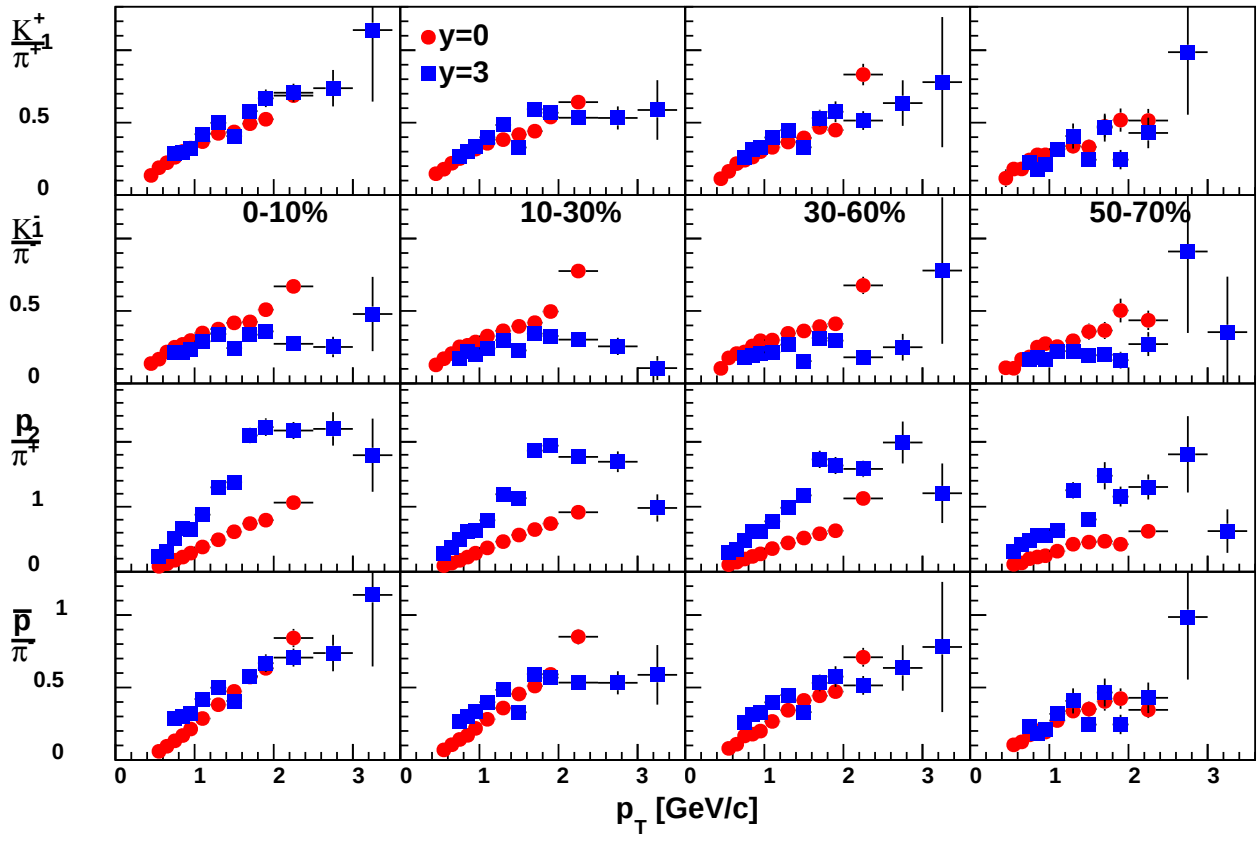

FIG. 9. Particle ratios from Cu+Cu collisions at $\sqrt{s_{NN}} = 200$ GeV as a function of p_T, at $y \sim 0$ (circle) and $y \sim 3$ (square) for various centralities. The centrality decreases from left to right.

sponding $\frac{\bar{p}}{\pi^-}$ ratio by almost a factor of 6. This has also been observed in Au+Au collisions at the same energy. While the beam protons may be contributing to the $\frac{p}{\pi^+}$ ratio, the reason for such large difference between the positive and negative baryon to meson ratios is not yet well understood. At both $y \sim 0$ and $y \sim 3$ the baryon to meson ratio increase with N_{part}. This is unexpected considering that baryons are supposed to come from gluons and pions from quarks. Due to their large couplings gluons lose more energy than quarks resulting in a reduced production of baryons compared to pions. As a result one expects the $\frac{\bar{p}}{\pi^-}$ ratio to be lower in central Cu+Cu collisions than in peripheral collisions, which is opposite to what is observed. The results are consistent with the observation that the R_{AA} values indicate mesons become more suppressed for central events, while R_{AA} values for baryons shows little centrality dependence.

IV. CONCLUSIONS

BRAHMS has measured transverse-momentum spectra, yields and ratios for identified charged hadrons $(\pi^{\pm}, K^{\pm}, p, \bar{p})$ in $\sqrt{s_{NN}} = 200$ GeV Cu+Cu collisions at y = 0 and y = 3 as a function of collision centrality. Following the assumption that a thermally equilibrated flowing bulk medium can be described within the framework of the hydrodynamic model, a simultaneous blast wave fit to the data was used to extract the kinetic freeze-out parameters T_{kin} and $\langle\beta\rangle$. As N_{part} increases T_{kin} falls while $\langle\beta\rangle$ increases at both central and forward rapidity. For a given value of $\langle\beta\rangle$ T_{kin} is about 15 MeV smaller at y = 3 than at y = 0. There does not seem to be a universal scaling of either T_{kin} or $\langle\beta\rangle$ with the total particle density.

For Cu+Cu collisions the scaled particles yields,

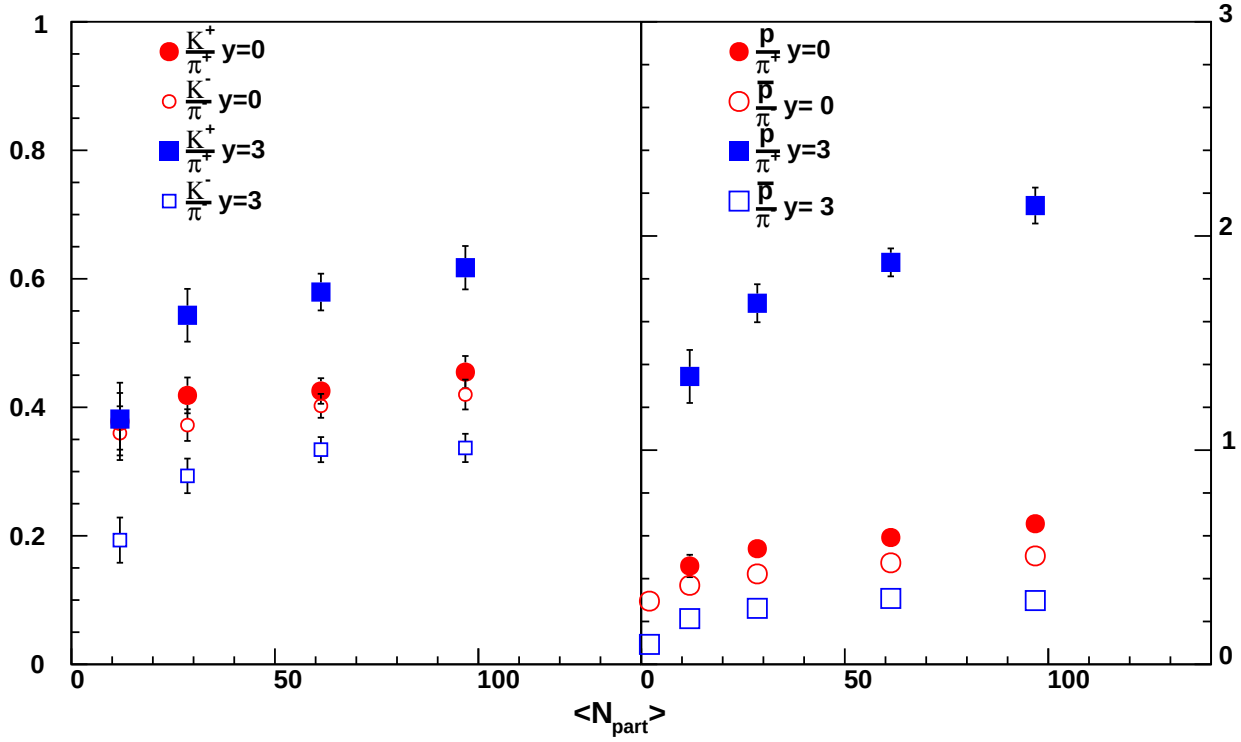

FIG. 10. Ratio of particle yields, $\frac{K}{\pi}$ (left) and $\frac{p}{\pi}$ (right) as a function of N_{part} for Cu+Cu collisions at $\sqrt{s_{NN}} = 200$ GeV. Before division the individual spectra have been integrated over $1.3 < p_T < 2.0$ GeV/c for y = 0 and over $1.5 < p_T < 3.0$ GeV/c for y = 3. Red circles denote y = 0 and blue squares y = 3. Solid symbols represent ratios of positive particles while open symbols show the ratios of negative particles.

$\frac{1}{(0.5*N_{part})}\frac{dN}{dy}$ rise with N_{part} up to $N_{part} \approx 50$ and then level off. The Au+Au scaled particle yields increase more slowly with N_{part}. This may reflect the smaller fraction of "corona" in central Cu+Cu collisions compared to peripheral Au+Au collisions [5].

The $\langle p_T \rangle$ of protons and antiprotons rises with N_{part} at both central and forward rapidity. There is a slight rise for kaons while the pion $\langle p_T \rangle$ is independent of N_{part}. The increase of $\langle p_T \rangle$ with mass is suggestive of radial flow. This effect is significantly weaker at forward rapidity.

Pion and kaon yields for $1.5 < p_T < 2.5$ are suppressed relative to scaled pp collisions. This suppression is strongest for the most central collisions. The suppression of the kaons is somewhat less than that of the pions. Even though the particle density decreases at forward rapidities, the meson suppression pattern remains similar to what is observed at mid rapidity. For $p_T > 1.3$ GeV the baryons from Cu+Cu collisions are enhanced relative to pp collisions at the same energy. This enhancement depends strongly on p_T but only weakly on centrality. It is significantly larger at y = 0 compared to y = 3. At central rapidity the protons and antiprotons have behave similarly but at y = 3 R_{AA} is significantly larger for antiprotons than protons.

The BRAHMS Cu+Cu data essentially cover the intermediate p_T region ($2 < p_T < 5$ GeV/c) which is expected to be influenced by the interplay between fragmentation and recombination, i.e., the fragmentation process may be altered by the surrounding environment [34]. The significant meson suppression in this p_T region measured by BRAHMS can be used to test parton fragmentation + recombination/coalescence [28–30, 35] models which have been found to describe very well particle production in the intermediate p_T region. At RHIC energies, hard parton scattering has been found to dominate the spectrum at high p_T ($p_T > 6$ GeV/c) and to be significantly

modified in A-A collisions (jet quenching). In this transverse momentum region, models incorporating perturbative QCD (pQCD) coupled with soft physics and energy loss [31] have demonstrated that fragmentation functions play an important role in hadron production [36]. The current results suggest that hard processes may also have a significant influence in the intermediate p_T region.

The $\frac{\pi^-}{\pi^+}$, $\frac{K^-}{K^+}$ and $\frac{\bar{p}}{p}$ ratios show no significant dependence on centrality or p_T but they do depend upon rapidity, presumably because of the higher baryon density in the forward region. At central rapidity the Cu+Cu results are consistent within errors with those measured in Au+Au collisions at the same energy.

The $\frac{K^{\pm}}{\pi^{\pm}}$ ratios increase with p_T up to $p_T = 1.6$ GeV/c before leveling off. They rise slowly with N_{part} at mid rapidity. This increase with N_{part} is more pronounced at forward rapidity. The slight excess of $\frac{K^+}{\pi^+}$ over $\frac{K^-}{\pi^-}$ at mid rapidity and the much larger excess at forward rapidity may be due to the non-zero net baryon density which favors associated production of K^+ over K^- at y = 3.

The $\frac{p}{\pi^+}$ and $\frac{\bar{p}}{\pi^-}$ ratios increase with p_T up to $p_T =$ 2.0 GeV/c before leveling off. This is most dramatic for the protons at forward rapidity. In the intermediate p_T region an enhancement of baryons over mesons is observed at both rapidities. This enhancement increases with N_{part}. The $\frac{p}{\pi^+}$ and $\frac{\bar{p}}{\pi^-}$ are similar at y = 0 but very different at y = 3. While pQCD calculations underestimate the baryon to meson ratio by a large factor,the coalescence/recombination [28–30] mechanism and baryon junction transport [31–33] are found to describe well the measured baryon to meson ratio at mid-rapidity in the intermediate p_T region ($2 < p_T < 6$ GeV/c) in Au+Au collisions. The coalescence/recombination model assumes a thermalized flowing partonic medium with an exponential spectrum at smaller p_T and a spectrum of hard scattered partons described by parton fragmentation functions or power law functions dominating at higher p_T.

Understanding the underlying mechanisms responsible for hadron production over the whole range of transverse momentum and rapidity accessible at RHIC and providing a consistent description of all the various aspects of the hadron spectra in heavy ion collisions remains to be a major challenge of RHIC physics. The current data should help to constrain theoretical attempts to reach this synthesis.

V. ACKNOWLEDGEMENTS

This work was supported by the office of Nuclear Physics of the U.S. Department of energy, the Danish Natural Science Research Council, the Research Council of Norway, the Polish State Committee for Scientific Research (KBN), and the Romanian Ministry of Research.

[1] I. Arsene *et al.* (BRAHMS Collaboration), Nucl.Phys. **A757**, 1 (2005), arXiv:nucl-ex/0410020 [nucl-ex].

[2] K. Adcox *et al.* (PHENIX Collaboration), Nucl.Phys. **A757**, 184 (2005), arXiv:nucl-ex/0410003 [nucl-ex].

[3] B. Back, M. Baker, M. Ballintijn, D. Barton, B. Becker, *et al.*, Nucl.Phys. **A757**, 28 (2005), arXiv:nucl-ex/0410022 [nucl-ex].

[4] J. Adams *et al.* (STAR Collaboration), Nucl.Phys. **A757**, 102 (2005), arXiv:nucl-ex/0501009 [nucl-ex].

[5] F. Becattini and J. Manninen, Phys.Lett. **B673**, 19 (2009), arXiv:0811.3766 [nucl-th].

[6] M. Adamczyk *et al.* (BRAHMS Collaboration), Nucl.Instrum.Meth. **A499**, 437 (2003).

[7] C. Adler, A. Denisov, E. Garcia, M. J. Murray, H. Strobele, *et al.*, Nucl.Instrum.Meth. **A470**, 488 (2001), arXiv:nucl-ex/0008005 [nucl-ex].

[8] B. Tomasik, U. A. Wiedemann, and U. W. Heinz, Heavy Ion Phys. **17**, 105 (2003), arXiv:nucl-th/9907096 [nucl-th].

$y = 0$	$\frac{dN}{dy}$	$(\frac{dN}{dy})_m$	$(\frac{dN}{dy})_m/\frac{dN}{dy}$	$\frac{dN}{dy}$	$(\frac{dN}{dy})_m$	$(\frac{dN}{dy})_m/\frac{dN}{dy}$	$\langle p_T \rangle$
Cent.	π^-			π^+			
$0-10\%$	72.0 ± 2.4	47.27 ± 0.92	66%	73.0 ± 2.4	48.40 ± 0.95	66%	477.4 ± 7.6
$10-30\%$	40.26 ± 0.95	26.70 ± 0.43	66%	41.47 ± 0.98	28.08 ± 0.46	68%	479.1 ± 5.9
$30-50\%$	17.30 ± 0.18	11.82 ± 0.27	68%	18.04 ± 0.19	12.53 ± 0.29	69%	482.9 ± 4.2
$50-70\%$	6.18 ± 0.34	4.43 ± 0.18	72%	6.45 ± 0.36	4.67 ± 0.19	72%	484 ± 14
	K^-			K^+			
$0-10\%$	11.67 ± 0.60	8.04 ± 0.15	69%	12.82 ± 0.66	8.78 ± 0.17	68%	674 ± 10
$10-30\%$	6.65 ± 0.24	4.38 ± 0.07	66%	7.32 ± 0.27	4.91 ± 0.08	67%	656.2 ± 7.4
$30-50\%$	2.92 ± 0.04	1.79 ± 0.04	61%	3.22 ± 0.05	1.98 ± 0.05	61%	632.0 ± 5.3
$50-70\%$	0.89 ± 0.07	0.56 ± 0.03	62%	1.14 ± 0.09	0.70 ± 0.06	61%	608 ± 17
	$\bar{p}$			p			
$0-10\%$	5.84 ± 0.45	4.63 ± 0.08	79%	7.75 ± 0.60	6.15 ± 0.11	79%	948 ± 12
$10-30\%$	3.46 ± 0.19	2.62 ± 0.04	76%	4.54 ± 0.24	3.46 ± 0.05	76%	904 ± 10
$30-50\%$	1.56 ± 0.03	1.13 ± 0.02	72%	2.13 ± 0.04	1.54 ± 0.03	72%	839.6 ± 6.6
$50-70\%$	0.60 ± 0.07	0.42 ± 0.02	70%	0.74 ± 0.09	0.51 ± 0.02	69%	779 ± 22

TABLE III. Results at y = 0 extracted from simultaneous blast wave fits for pions, kaons, (anti)protons. The results are averages over six fit ranges.

$y = 3$	$\frac{dN}{dy}$	$(\frac{dN}{dy})_m$	$(\frac{dN}{dy})_m/\frac{dN}{dy}$	$\frac{dN}{dy}$	$(\frac{dN}{dy})_m$	$(\frac{dN}{dy})_m/\frac{dN}{dy}$	$\langle p_T \rangle$
Cent.	π^-			π^+			
$0-10\%$	29.18 ± 0.92	12.24 ± 0.67	42%	28.38 ± 0.89	9.54 ± 0.17	34%	437.7 ± 6.9
$10-30\%$	17.34 ± 0.28	8.62 ± 0.44	50%	15.71 ± 0.25	5.56 ± 0.08	35%	462.0 ± 3.9
$30-50\%$	8.75 ± 0.24	3.89 ± 0.28	44%	7.89 ± 0.21	2.60 ± 0.06	33%	442.2 ± 6.1
$50-70\%$	3.01 ± 0.10	1.47 ± 0.18	49%	2.72 ± 0.09	1.00 ± 0.04	37%	468.9 ± 7.8
	K^-			K^+			
$0-10\%$	3.92 ± 0.19	1.15 ± 0.03	29%	5.40 ± 0.27	1.57 ± 0.03	29%	569.0 ± 8.6
$10-30\%$	2.35 ± 0.06	0.69 ± 0.01	29%	3.39 ± 0.08	0.98 ± 0.02	29%	570.3 ± 4.5
$30-50\%$	1.06 ± 0.04	0.28 ± 0.01	27%	1.60 ± 0.07	0.42 ± 0.01	26%	547.6 ± 7.2
$50-70\%$	0.37 ± 0.02	0.10 ± 0.01	27%	0.47 ± 0.02	0.13 ± 0.01	27%	553.7 ± 8.7
	$\bar{p}$			p			
$0-10\%$	1.13 ± 0.09	0.79 ± 0.02	70%	7.22 ± 0.55	5.51 ± 0.04	76%	765 ± 12
$10-30\%$	0.85 ± 0.03	0.58 ± 0.01	69%	4.63 ± 0.16	3.40 ± 0.02	74%	737.0 ± 6.1
$30-50\%$	0.38 ± 0.02	0.25 ± 0.01	66%	2.10 ± 0.13	1.53 ± 0.02	73%	707 ± 10
$50-70\%$	0.15 ± 0.01	0.10 ± 0.01	65%	0.82 ± 0.06	0.61 ± 0.01	74%	687 ± 11

TABLE IV. Results at y = 3 extracted from simultaneous blast wave fits for pions, kaons, (anti)protons. The results are averages over six fit ranges.

[9] G. Agakishiev *et al.* (STAR Collaboration), Phys.Rev.Lett. **108**, 072301 (2012), arXiv:1107.2955 [nucl-ex].

[10] M. Aggarwal *et al.* (STAR Collaboration), Phys.Rev. **C84**, 034909 (2011), arXiv:1006.1961 [nucl-ex].

[11] K. Adcox *et al.* (PHENIX Collaboration), Phys.Rev.Lett. **88**, 022301 (2002), arXiv:nucl-ex/0109003 [nucl-ex].

[12] C. Adler *et al.* (STAR Collaboration), Phys.Rev.Lett. **89**, 202301 (2002), arXiv:nucl-ex/0206011 [nucl-ex].

[13] I. Arsene *et al.* (BRAHMS Collaboration), Phys.Rev.Lett. **91**, 072305 (2003), arXiv:nucl-ex/0307003 [nucl-ex].

[14] B. Back *et al.* (PHOBOS Collaboration), Phys.Lett. **B578**, 297 (2004), arXiv:nucl-ex/0302015 [nucl-ex].

[15] S. Adler *et al.* (PHENIX Collaboration), Phys.Rev.Lett. **91**, 072301 (2003), arXiv:nucl-ex/0304022 [nucl-ex].

[16] J. Adams *et al.* (STAR Collaboration), Phys.Rev.Lett. **91**, 172302 (2003), arXiv:nucl-ex/0305015 [nucl-ex].

$y=0$	π^- (p_T *Exp.*)				π^+ (p_T *Exp.*)			
Cent.	$\frac{dN}{dy}$	T	$\langle p_T \rangle$	$\frac{\chi^2}{d.o.f}$	$\frac{dN}{dy}$	T	$\langle p_T \rangle$	$\frac{\chi^2}{d.o.f}$
$0-10\%$	68.3 ± 2.8	242.3 ± 4.6	484.6 ± 9.3	7.2/7	71.3 ± 2.9	238.3 ± 4.5	476.6 ± 9.1	7.8/7
$10-30\%$	38.3 ± 1.4	241.7 ± 4.3	483.5 ± 8.7	11.6/7	40.4 ± 1.5	238.7 ± 4.2	477.4 ± 8.5	12.2/7
$30-50\%$	17.0 ± 0.8	238.2 ± 5.0	476 ± 10	8.8/7	18.2 ± 0.8	235.4 ± 4.9	470.8 ± 9.8	8.7/7
$50-70\%$	6.41 ± 0.44	231.2 ± 7.1	462 ± 14	6.04/7	6.82 ± 0.47	229.3 ± 6.9	459 ± 14	6.03/7
	π^- (m_T *Exp.*)				π^+ (m_T *Exp.*)			
$0-10\%$	64.9 ± 2.5	239.2 ± 4.6	501.1 ± 9.0	8.6/7	67.6 ± 2.7	235.2 ± 4.5	493.4 ± 8.8	9.3/7
$10-30\%$	36.4 ± 1.3	238.7 ± 4.3	500.0 ± 8.4	13.5/7	38.3 ± 1.4	235.7 ± 4.2	494.3 ± 8.2	14.2/7
$30-50\%$	16.1 ± 0.7	235.1 ± 5.0	493.2 ± 9.7	10.3/7	17.3 ± 0.8	232.4 ± 4.9	487.9 ± 9.5	10.1/7
$50-70\%$	6.1 ± 0.4	228.3 ± 7.0	480 ± 14	6.9/7	6.4 ± 0.4	226.3 ± 6.9	476 ± 13	6.8/7
	π^- (*Power law*)				π^+ (*Power law*)			
Cent.	$\frac{dN}{dy}$	n	$\langle p_T \rangle$	$\frac{\chi^2}{d.o.f}$	$\frac{dN}{dy}$	n	$\langle p_T \rangle$	$\frac{\chi^2}{d.o.f}$
$0-10\%$	80.3 ± 8.5	15.6 ± 4.6	449 ± 22	0.34/7	88 ± 10	13.4 ± 3.4	432 ± 23	0.12/7
$10-30\%$	45.5 ± 4.6	14.6 ± 3.7	446 ± 21	1.30/7	50.4 ± 5.5	12.9 ± 2.8	430 ± 22	0.47/7
$30-50\%$	21.8 ± 3.0	11.6 ± 2.8	424 ± 27	0.26/7	23.3 ± 3.2	12.2 ± 3.0	419 ± 26	0.09/7
$50-70\%$	8.5 ± 1.8	11.1 ± 3.6	404 ± 40	0.14/7	9.1 ± 1.9	11.2 ± 3.5	399 ± 39	0.83/7
$y=3$	π^- (p_T *Exp.*)				π^+ (p_T *Exp.*)			
Cent.	$\frac{dN}{dy}$	T	$\langle p_T \rangle$	$\frac{\chi^2}{d.o.f}$	$\frac{dN}{dy}$	T	$\langle p_T \rangle$	$\frac{\chi^2}{d.o.f}$
$0-10\%$	28.2 ± 1.2	217.5 ± 3.6	435.1 ± 7.2	4.28/7	27.8 ± 1.4	216.1 ± 4.0	432.2 ± 8.0	17.3/7
$10-30\%$	18.45 ± 0.77	219.6 ± 3.5	439.3 ± 6.9	4.44/7	15.71 ± 0.69	225.9 ± 4.0	451.7 ± 7.9	8.91/7
$30-50\%$	9.04 ± 0.46	212.2 ± 4.1	424.5 ± 8.1	14.1/7	7.62 ± 0.42	217.7 ± 4.6	435.5 ± 9.2	9.27/7
$50-70\%$	3.21 ± 0.22	220.5 ± 6.1	441 ± 12	7.65/7	3.00 ± 0.23	215.9 ± 6.2	432 ± 12	19.4/7
	π^- (m_T *Exp.*)				π^+ (m_T *Exp.*)			
$0-10\%$	26.3 ± 1.1	215.0 ± 3.6	454.0 ± 6.9	4.50/7	25.8 ± 1.2	213.7 ± 4.0	451.5 ± 7.7	18.5/7
$10-30\%$	17.25 ± 0.68	217.1 ± 3.5	458.1 ± 6.7	4.86/7	14.74 ± 0.62	223.3 ± 4.0	470.2 ± 7.7	9.76/7
$30-50\%$	8.41 ± 0.41	209.7 ± 4.0	443.8 ± 7.9	14.9/7	7.10 ± 0.37	215.3 ± 4.6	454.6 ± 8.9	10.2/7
$50-70\%$	3.00 ± 0.20	218.0 ± 6.1	460 ± 12	8.09/7	2.81 ± 0.20	213.3 ± 6.2	451 ± 12	19.2/7
	π^- (*Power law*)				π^+ (*Power law*)			
Cent.	$\frac{dN}{dy}$	n	$\langle p_T \rangle$	$\frac{\chi^2}{d.o.f}$	$\frac{dN}{dy}$	n	$\langle p_T \rangle$	$\frac{\chi^2}{d.o.f}$
$0-10\%$	37.1 ± 3.2	17.4 ± 2.8	382 ± 14	15.5/8	40.3 ± 4.2	16.2 ± 2.4	366 ± 16	9.47/8
$10-30\%$	22.6 ± 1.7	22.7 ± 4.5	398 ± 12	18.1/8	19.8 ± 1.6	20.9 ± 4.0	403 ± 13	20.5/8
$30-50\%$	12.8 ± 1.4	15.6 ± 2.5	362 ± 16	18.3/8	10.5 ± 1.2	16.6 ± 3.0	377 ± 17	8.45/8
$50-70\%$	3.98 ± 0.52	21.2 ± 6.9	400 ± 22	5.61/8	4.02 ± 0.60	16.5 ± 4.2	380 ± 23	19.9/8

TABLE V. Extracted fit results for pions. The fit range is $0.4 < p_T < 1.6$ GeV/c for the exponential fits and $0.5 < p_T < 2.0$ GeV/c for the power law fits

[17] A. Adare *et al.* (PHENIX Collaboration), Phys.Rev.Lett. **98**, 172301 (2007), arXiv:nucl-ex/0611018 [nucl-ex].

[18] G. Aad *et al.* (Atlas Collaboration), Phys.Rev.Lett. **105**, 252303 (2010), arXiv:1011.6182 [hep-ex].

[19] S. Chatrchyan *et al.* (CMS Collaboration), Phys.Rev. **C84**, 024906 (2011), arXiv:1102.1957 [nucl-ex].

[20] G. Aad *et al.* (ATLAS Collaboration), Phys.Lett. **B719**, 220 (2013), arXiv:1208.1967 [hep-ex].

[21] S. Chatrchyan *et al.* (CMS Collaboration), JHEP **1210**, 087 (2012), arXiv:1205.5872 [nucl-ex].

[22] S. Adler *et al.* (PHENIX Collaboration), Phys.Rev.Lett. **91**, 072303 (2003), arXiv:nucl-ex/0306021 [nucl-ex].

[23] J. Adams *et al.* (STAR Collaboration), Phys.Rev.Lett. **91**, 072304 (2003), arXiv:nucl-ex/0306024 [nucl-ex].

[24] I. Arsene *et al.* (BRAHMS Collaboration), Phys.Rev.Lett. **93**, 242303 (2004), arXiv:nucl-ex/0403005 [nucl-ex].

[25] M. C. for the ALICE Collaboration, in *Proceedings of Strange Quark Matter 2013* (2013).

$y=0$	K^- (p_T *Exp.*)				K^+ (p_T *Exp.*)			
Cent.	$\frac{dN}{dy}$	T	$\langle p_T \rangle$	$\frac{\chi^2}{d.o.f}$	$\frac{dN}{dy}$	T	$\langle p_T \rangle$	$\frac{\chi^2}{d.o.f}$
$0-10\%$	12.54 ± 0.40	321.7 ± 7.5	643 ± 15	4.02/7	13.77 ± 0.45	317.8 ± 7.3	636 ± 15	5.88/7
$10-30\%$	6.85 ± 0.20	318.2 ± 6.8	636 ± 14	4.94/7	7.81 ± 0.24	310.3 ± 6.6	621 ± 13	2.34/7
$30-50\%$	2.79 ± 0.10	315.3 ± 8.0	631 ± 16	12.3/7	3.11 ± 0.12	314.0 ± 8.2	628 ± 16	7.31/7
$50-70\%$	0.85 ± 0.05	318 ± 14	636 ± 27	6.40/7	1.21 ± 0.09	284 ± 12	568 ± 24	2.13/7
	K^- (m_T *Exp.*)				K^+ (m_T *Exp.*)			
$0-10\%$	11.23 ± 0.33	280.8 ± 6.9	682 ± 13	1.52/7	12.32 ± 0.37	277.3 ± 6.7	676 ± 13	1.24/7
$10-30\%$	6.12 ± 0.17	277.5 ± 6.3	676 ± 12	2.31/7	6.92 ± 0.19	271.3 ± 6.1	664 ± 12	0.81/7
$30-50\%$	2.50 ± 0.09	274.3 ± 7.4	670 ± 14	6.74/7	2.78 ± 0.10	273.7 ± 7.5	669 ± 14	2.86/7
$50-70\%$	0.75 ± 0.04	279 ± 13	680 ± 24	5.32/7	1.02 ± 0.07	252 ± 11	626 ± 21	1.81/7
	K^- (m_T *Boltz.*)				K^+ (m_T *Boltz.*)			
$0-10\%$	10.71 ± 0.31	222.3 ± 4.6	691 ± 13	3.90/7	11.75 ± 0.35	220.3 ± 4.4	686 ± 12	2.14/7
$10-30\%$	5.83 ± 0.16	220.2 ± 4.2	685 ± 12	5.68/7	6.59 ± 0.19	216.5 ± 4.1	675 ± 11	4.38/7
$30-50\%$	2.39 ± 0.08	218.1 ± 4.9	680 ± 13	6.58/7	2.65 ± 0.09	218 ± 5.0	679 ± 14	3.17/7
$50-70\%$	0.71 ± 0.04	222.2 ± 8.3	691 ± 23	5.41/7	0.96 ± 0.06	205.1 ± 7.6	644 ± 21	2.34/7
$y=3$	K^- (p_T *Exp.*)				K^+ (p_T *Exp.*)			
$0-10\%$	5.29 ± 0.38	242.0 ± 6.9	484 ± 14	8.31/4	5.85 ± 0.36	267.7 ± 7.8	535 ± 16	5.74/4
$10-30\%$	3.05 ± 0.21	246.0 ± 6.8	492 ± 14	6.00/4	3.88 ± 0.23	258.6 ± 6.8	517 ± 14	9.68/4
$30-50\%$	1.53 ± 0.15	225.2 ± 8.0	450 ± 16	2.55/4	1.79 ± 0.14	249.4 ± 8.1	498 ± 16	8.21/4
$50-70\%$	0.44 ± 0.06	250 ± 16	501 ± 32	1.69/4	0.50 ± 0.07	262 ± 16	523 ± 33	5.64/4
	K^- (m_T *Exp.*)				K^+ (m_T *Exp.*)			
$0-10\%$	3.75 ± 0.19	227.7 ± 4.6	580.1 ± 9.0	12.6/6	4.45 ± 0.19	249.8 ± 4.7	622.7 ± 9.1	8.01/6
$10-30\%$	2.18 ± 0.10	231.5 ± 4.9	587.6 ± 8.6	7.70/6	2.86 ± 0.12	244.9 ± 4.3	613.4 ± 8.3	11.2/6
$30-50\%$	0.97 ± 0.07	220.3 ± 6.1	566 ± 12	12.5/6	1.26 ± 0.07	239.7 ± 5.5	603 ± 11	13.0/6
$50-70\%$	0.34 ± 0.03	220.4 ± 9.3	566 ± 18	1.93/6	0.39 ± 0.03	239.6 ± 9.6	603 ± 18	6.51/6
	K^- (m_T *Boltz.*)				K^+ (m_T *Boltz.*)			
$0-10\%$	3.31 ± 0.17	193.9 ± 3.5	613 ± 9.5	14.4/6	3.95 ± 0.17	210.4 ± 3.5	658.3 ± 9.5	10.8/6
$10-30\%$	1.93 ± 0.09	196.9 ± 3.4	621.6 ± 9.2	10.2/6	2.54 ± 0.11	206.8 ± 3.2	648.4 ± 8.8	13.6/6
$30-50\%$	0.86 ± 0.06	188.1 ± 4.6	597 ± 13	15.6/6	1.12 ± 0.06	202.6 ± 4.1	637 ± 11	15.5/6
$50-70\%$	0.30 ± 0.03	188.9 ± 7.0	600 ± 20	1.44/6	0.34 ± 0.03	203.2 ± 7.1	639 ± 20	6.72/6

TABLE VI. Extracted fit results for kaons. The fit range is $0.4 < p_T < 1.6$ GeV/c at y=0 and $0.7 < p_T < 1.6$ GeV/c at y=3

[26] M. Djordjevic and M. Djordjevic(2013), arXiv:1307.4714 [nucl-th].

[27] B. Abelev *et al.* (STAR Collaboration), Phys.Rev. **C81**, 054907 (2010), arXiv:0911.3130 [nucl-ex].

[28] V. Greco, C. Ko, and P. Levai, Phys.Rev. **C68**, 034904 (2003), arXiv:nucl-th/0305024 [nucl-th].

[29] R. Fries, B. Muller, C. Nonaka, and S. Bass, Phys.Rev. **C68**, 044902 (2003), arXiv:nucl-th/0306027 [nucl-th].

[30] V. Greco, C. Ko, and I. Vitev, Phys.Rev. **C71**, 041901 (2005), arXiv:nucl-th/0412043 [nucl-th].

[31] I. Vitev and M. Gyulassy, Phys. Rev. C **65**, 041902 (Apr 2002), http://link.aps.org/doi/10.1103/PhysRevC.65.041902.

[32] I. Vitev and M. Gyulassy, Nucl.Phys. **A715**, 779 (2003), arXiv:hep-ph/0208108 [hep-ph].

[33] V. Topor Pop, M. Gyulassy, J. Barrette, C. Gale, S. Vance, *et al.*, Phys.Rev. **C68**, 054902 (2003), arXiv:nucl-th/0209089 [nucl-th].

[34] X.-f. Guo and X.-N. Wang, Phys.Rev.Lett. **85**, 3591 (2000), arXiv:hep-ph/0005044 [hep-ph].

[35] R. C. Hwa and C. Yang, Phys.Rev. **C70**, 024905 (2004), arXiv:nucl-th/0401001 [nucl-th].

[36] X. Zhang, G. Fai, and P. Lévai, Phys. Rev. Lett. **89**, 272301 (Dec 2002), http://link.aps.org/doi/10.1103/PhysRevLett.89.272301.

$y = 0$	$\bar{p}$ (m_T *Exp.*)				p (m_T *Exp.*)			
Cent.	$\frac{dN}{dy}$	T	$\langle p_T \rangle$	$\frac{\chi^2}{d.o.f}$	$\frac{dN}{dy}$	T	$\langle p_T \rangle$	$\frac{\chi^2}{d.o.f}$
$0-10\%$	6.06 ± 0.15	345.3 ± 7.8	933 ± 15	$10.5/8$	8.14 ± 0.20	335.1 ± 7.4	913 ± 15	$6.69/8$
$10-30\%$	3.52 ± 0.08	324.1 ± 6.6	892 ± 13	$3.47/8$	4.67 ± 0.11	317.1 ± 6.3	878 ± 12	$1.19/8$
$30-50\%$	1.55 ± 0.05	296.4 ± 7.1	837 ± 14	$4.49/8$	2.15 ± 0.07	288.4 ± 6.7	821 ± 13	$0.96/8$
$50-70\%$	0.59 ± 0.03	264.2 ± 9.5	773 ± 19	$4.90/8$	0.73 ± 0.04	260.6 ± 8.4	766 ± 17	$2.06/8$
	$\bar{p}$ (m_T *Boltz.*)				p (m_T *Boltz.*)			
$0-10\%$	5.96 ± 0.15	282.2 ± 5.3	923 ± 14	$6.38/8$	8.01 ± 0.20	275.3 ± 5.1	906 ± 14	$3.79/8$
$10-30\%$	3.45 ± 0.08	267.9 ± 4.6	888 ± 12	$1.84/8$	4.59 ± 0.11	263.0 ± 4.5	876 ± 12	$0.57/8$
$30-50\%$	1.52 ± 0.05	248.7 ± 5.1	840 ± 14	$5.6/8$	2.10 ± 0.06	242.9 ± 4.9	825 ± 13	$2.43/8$
$50-70\%$	0.58 ± 0.03	225.6 ± 7.1	780 ± 19	$6.48/8$	0.72 ± 0.04	223.1 ± 6.3	773 ± 17	$2.40/8$
$y = 3$	$\bar{p}$ (m_T *Exp.*)				p (m_T *Exp.*)			
$0-10\%$	1.19 ± 0.04	248.1 ± 4.6	740.6 ± 9.3	$10.4/8$	7.09 ± 0.15	263.2 ± 3.5	771.0 ± 7.0	$12.5/8$
$10-30\%$	0.88 ± 0.03	238.1 ± 4.3	720.4 ± 8.7	$16.7/8$	4.39 ± 0.09	254.9 ± 3.3	754.2 ± 6.7	$12.8/8$
$30-50\%$	0.38 ± 0.01	231.5 ± 5.2	707 ± 11	$12.1/8$	1.96 ± 0.04	242.2 ± 3.4	728.7 ± 6.8	$20.3/8$
$50-70\%$	0.15 ± 0.01	217.2 ± 7.9	678 ± 16	$18.4/8$	0.77 ± 0.02	229.7 ± 3.9	703.2 ± 7.9	$23.7/8$
	$\bar{p}$ (m_T *Boltz.*)				p (m_T *Boltz.*)			
$0-10\%$	1.16 ± 0.04	214.0 ± 3.5	749.5 ± 9.3	$12.3/8$	6.94 ± 0.14	224.8 ± 2.6	777.9 ± 7.0	$14.9/8$
$10-30\%$	0.86 ± 0.03	206.4 ± 3.3	729.6 ± 8.8	$22.2/8$	4.30 ± 0.09	218.6 ± 2.5	761.7 ± 6.7	$17.2/8$
$30-50\%$	0.36 ± 0.01	201.4 ± 4.1	716 ± 11	$15.5/8$	1.91 ± 0.04	209.3 ± 2.6	737.2 ± 6.9	$29.1/8$
$50-70\%$	0.15 ± 0.01	190.5 ± 6.3	688 ± 17	$20.1/8$	0.75 ± 0.02	199.5 ± 3.0	711.5 ± 8.0	$31.6/8$

TABLE VII. Extracted fit results for protons and anti-protons. The fit range is $0.5 < p_T < 2.0$ GeV/c.